Journal of Manufacturing Processes 68 (2021) 750–760

Contents lists available at ScienceDirect

Journal of Manufacturing Processes

journal homepage: www.elsevier.com/locate/manpro

Prediction of the power supplied in friction-based joining process of metal-polymer hybrids through machine learning

F. Lambiase *, V. Grossi, S.I. Scipioni, A. Paoletti

Dept. of Industrial and Information Engineering and Economics, University of L'Aquila, via G. Gronchi 18, Zona Industriale di Pile, 67100, AQ, Italy

ARTICLE INFO

Keywords:
Multi-material joints
Hybrid joints
Friction-assisted joining
Machine learning
Artificial neural networks
Process design

ABSTRACT

This study analyses the influence of the key process parameters during friction assisted joining process on the frictional power. Experimental joining tests were performed by varying the plunging force, the tool rotation speed, and the tool diameter. During the tests, the main processing loads were acquired through an instrumented equipment. The physical correlation between the process parameters and the frictional power was determined and modeled through machine learning. Different model configurations were tested varying the number of neurons in the hidden layer. The results proved the possibility to predict the frictional power through machine learning with good reliability ($R^2 = 0.90$) and generalization capability. This was pursued using a limited number of experimental tests through a signal breakdown approach.

1. Introduction

Thermo-mechanical joining processes are a promising solution to produce hybrid multilateral joints [1]. These processes are based on softening a thin layer of the thermoplastic component at the metal-polymer interface. During thermo-mechanical joining processes, the two materials are heated to a temperature close to the melting/softening ranges of the polymer [2]. Then, the application of an external pressure enables the formation of the joint. Different joining mechanisms can develop, including physical bonding (van der Valls forces), chemical bonding (C-O-M bonds) [3], and also micro-mechanical interlocking [4] through surface roughness or process-induced surface asperities on the metal surface. The surface of the metal component can be functionalized to increase the strength of these joints. Several technological solutions have been proposed, e.g. anodization (for aluminum sheets) [5,6] plasma electrolytic oxidation [7,8], and laser texturing [9–14].

The mechanical strength of these joints is directly related to the temperature reached at the interface of the two components [15]. The temperature depends on the power absorbed during the joining process [16]. Previous studies investigated the influence of the process parameters on the strength of the joints using an almost "likely black-box" approach. Direct relationships between the process parameters and the joint's quality can be established by sophisticated models such as Artificial Neural Networks. However, this approach tends to hinder the causality involved in the process, how the material behaves and how to optimize the process outside the bounds of the analyzed processing window. A more "enlightened approach" would uncover such relationships by a breakdown of the cause-effect relationships, as schematized in Fig. 1.

This approach starts from the joints' quality and goes back to the influence of the process parameters; furthermore, it can be split into separate steps and more focused activities. This approach would produce larger amount of transferable knowledge as the process causality is pursued. Many studies investigated the influence of the joint's morphology on the mechanical behavior of the joints. It is crucial to determine which process condition is the most significant to trigger the bonding mechanism and the development of process-induced defects [17]. Finite element models [18] as well as artificial Intelligence based approaches would provide more insights for the prediction of the process conditions based on a selection of process parameters. The results reported in [14] for friction-assisted joining indicate that the temperature at the metal-polymer interface represents the key parameter. This confirms the close relationship between the temperature window and the mechanical behavior of the joints made by thermomechanical joining processes.

Direct temperature measurements at the metal-polymer interface are extremely complex. Thus, numerical [16] and machine learning-based models [19] have been developed to predict the temperature produced once the power supplied during the process is known. However, unlike laser joining processes [20–24], the power involved in friction-

* Corresponding author at: Monteluco di Roio, 67040, AQ, Italy.
E-mail address: francesco.lambiase@univaq.it (F. Lambiase).

https://doi.org/10.1016/j.jmapro.2021.06.001
Received 3 May 2021; Received in revised form 22 May 2021; Accepted 3 June 2021
Available online 17 June 2021

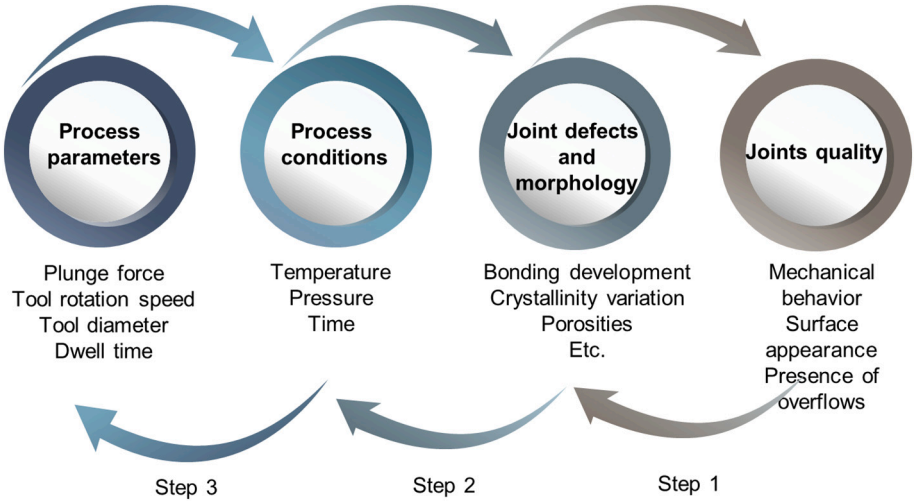

Fig. 1. Analysis steps towards friction-based joining process design and optimization.

based processes is not known a priori [25]. This problem is common to friction-based joining processes such as ultrasonic joining [26–34], friction spot joining [35–41], friction lap welding [5,42,43], friction stir lap welding [44–46], and friction riveting [47–49]. The knowledge of the relationship between the process parameters and the frictional power would greatly improve the selection of the process parameters. In addition, the frictional power also changes during the process owing to the variable heat exchanges with the environment and the surrounding clamping equipment and above all the variation (softening) of the flow stress on the metal in contact with the tool [19]. Thus, the prediction of the frictional power in the friction-based joining process is a challenging objective. Thus, the key demand for process design in friction-based joining processes is the possibility to predict the amount of frictional power once a set of process parameters is selected. This would represent the first step towards an engineered process design.

The present investigation is aimed at meeting such demand through the development of a model that predicts the frictional heat supplied when a given set of process parameters is adopted. This was pursued through the adoption of a machine learning modeling approach. To this end, an experimental campaign of joining tests was conducted using an instrumented equipment, which enabled the measurement of the force and torque during the process. The experiments involved different processing conditions, including the plunging force, the rotation speed, the tool diameter, and joining time. The measurements were elaborated, used to train, and validate a Machine Learning based model. Different configurations were tested to improve the generalization and accuracy capabilities of the developed model.

2. Materials and methods

Friction assisted joining process is a thermomechanical joining process that is used to produce lap joint between metal-polymer [2] and metal composite [50] thin components. During the process, the tool rotates at relatively high speeds (typical values range between 2000 and 8000 RPM) and slightly plunges the metal component with a relatively low plunging force (typically smaller than 1 kN). This enables the production of high frictional power with a small plunging imprint released by the tool on the metal sheets. The imprint is usually lower than 0.1 mm in depth. The frictional power enables to rapid heat of the tool-metal interface and the heat diffuses towards the metal-polymer interface. Then, the polymer gets softer for a certain thickness leading to the penetration of the artificial asperities (previously produced on the metal surface) within the polymer. This enables the formation of strong micro-mechanical interlocks. After the penetration, the tool rapidly retracts leading to the cooling and consolidation of the joint. The process parameters (those influencing the frictional power and those influencing the interaction time) have to be selected to provide sufficient energy to enable a thin layer of polymer to soften/melt. On the other hand, excess of energy should be avoided since it would involve excessive temperatures (and consequently process-induced defects, such as those reported in [17]), waste of energy, and higher joining time. A schematic of the main phases along with the joint development is depicted in Fig. 2.

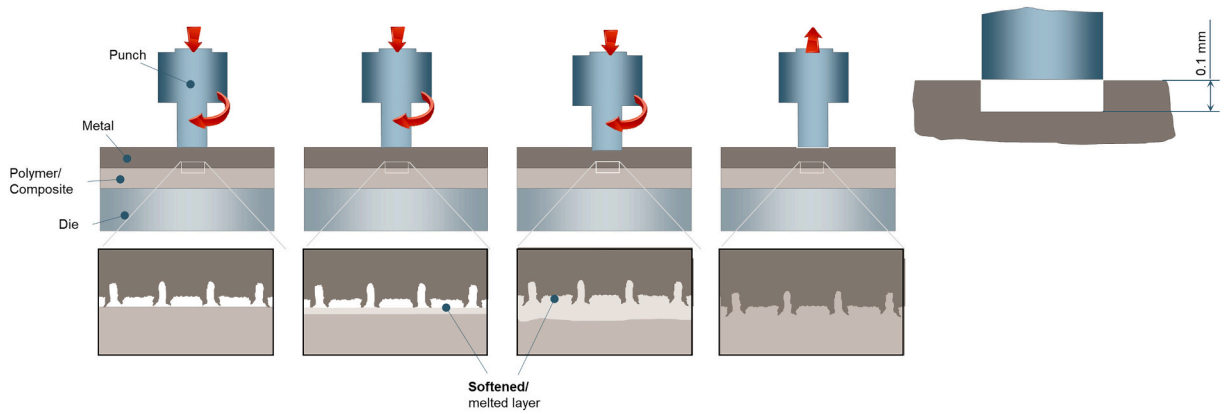

Fig. 2. Schematic of the joint formed by the frictional assisted joining process.

Table 1
Main physical and thermal characteristics of involved materials [17].

Material	Density [kg/m^3]	Glass transition [°C]	Melting point [°C]
PA66	1150	47	258
AA7075	2810	–	477–635 °C

2.1. Experimental details

A campaign of experimental tests was conducted using 3 mm thick sheets of aluminum AA7075 alloy and polyamide PA66 sheet (5 mm thick). The main physical characteristics of the materials involved are summarized in Table 1. The samples were cut into strips that were 25 mm wide and 80 mm long. The resulting area of overlap was 25 × 25 mm^2.

Experimental joining tests were conducted under prescribed plunging force (F_{max}) through a prototypal joining machine equipped with load and torque sensors. A schematic of the clamping system and the piezoelectric modules schematizing the experimental setup is depicted in Fig. 3. The machine was equipped with a spindle having a maximum power of 13.5 kW and a maximum rotational speed of 8000 RPM. Three tools with a cylindrical shape, flat end tooltip, and 0.1 mm corner radius were used. The tools differed by the tooltip diameters (D = 10 mm, D = 15 mm, and D = 20 mm), as also schematized in Fig. 3. The tools were made of Bohler K720 steel.

The joining process consisted of different phases. First, the tool was put in rotation at a prescribed speed (ω). Then, the tool was plunged against the metal sheet at a prescribed rate (1000 N/s) until the prescribed plunging force F_{max} was reached. Then, the tool continued plunging the metal (at the prescribed load F_{max}) as long as the dwell time elapsed. Finally, the tool was rapidly retracted from the metal (at 50 mm/s).

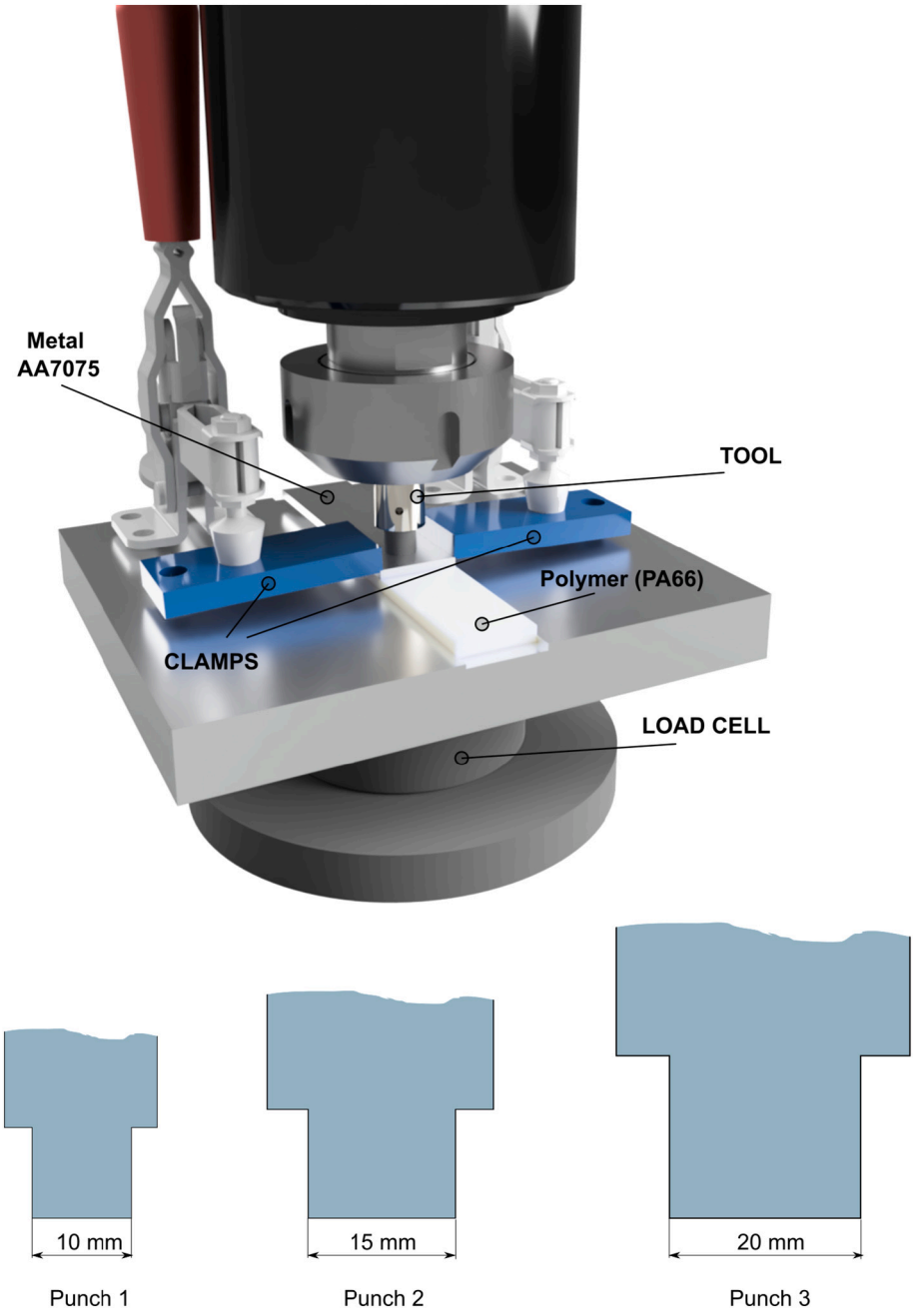

Fig. 3. Schematic of the equipment used to produce FAJ joints and main dimension of the tools adopted.

Table 2
Levels used for the experimental campaign.

Level	Tool diameter, D [mm]	Plunging force, F_{max} [N]	Rotation speed, ω [RPM]
I	10	150	2000
II	15	250	4000
III	20	350	6000
IV		450	8000
V		550	

The experimental campaign involved the variation of the tool diameter (D) rotation speed (ω), and the plunging force (F_{max}) over a full factorial plan 3 (D) × 5 (F_{max}) × 4 (ω). This led to 60 joining conditions. The joining experiments were conducted with a Dwell time D_t of 15 s. The choice of the adopted process parameters was based on typical values adopted for friction assisted joining process. The levels involved in the experimental plan are reported in Table 2.

During the experimental tests, the plunging force and the torque were acquired using two piezoelectric modules, Kistler model 9055-9063B and Kistler multichannel Model 5017 charging amplifier at a sample rate of 2.0 kHz. An I/O acquisition board model USB6009 by National Instrument was adopted for data acquisition.

2.2. Machine learning approach

For each processing condition, the plunging force and the frictional power were determined. To this end, the torque value (M_z) was multiplied by the tool rotation speed (ω) used in the test. The frictional power data were related to processing conditions through two layers of Artificial Neural Network (ANN), which was developed within the Matlab 2019b environment, as depicted in Fig. 4. Different network configurations were tested by varying the key parameters (mainly the number of neurons and the transfer functions). The "early-stopping" algorithm was adopted to avoid overfitting. Indeed, data was subdivided into separate sets, namely training, validation, and test sets. The training set was used to determine the weights and biases of the neural network. The validation set was adopted to trigger the onset of overfitting. Indeed, during the training, the overall error on the training and validation sets was monitored. The overall error that is computed on the training set is monotonically descended. However, since the model was not trained on the validation set, when the model tends to overfit the training data, the error computed on the validation set starts to increase. This triggers the early stopping of the Artificial Neural Network model. To this end, 20% of data were used for the training set, 50% for the validation set, and the remaining 30% for the test set. The samples used for the three datasets were selected randomly from the experimental database.

2.3. Data extraction

During the joining process, the torque M_z was measured using the above-mentioned piezoelectric cell. This enabled the calculation of the frictional power P as the product of M_z by ω (rotation speed). Then, the mean frictional power P, that is the energy provided for unit time, was determined using Eq. (1).

$$P(t^*) = \frac{1}{t^*}\int_0^{t^*} M_z\omega \, dt \tag{1}$$

Fig. 5 depicts schematically the approach used for data extraction from the experimental curves. For a given set of processing conditions, e.g. D=D*, $F_{max} = F_{max}$*, and ω = ω*, the experimental curve of P is calculated as $M_z \times \omega$. Then, the energy E_{t^*} supplied for a given interval of time t* was calculated as well as the mean frictional power $P_{t^*} = E_{t^*}/t^*$. Each experimental curve was consequently subdivided to provide the mean frictional power after given time intervals (between 0.5 s and 15 s with steps of 0.5 s). Thus, from each curve, up to 30 values of P were determined (for each joining time). This procedure was conducted for all the experimental curves measured during the joining tests performed with varying the process parameters (tool diameter, tool rotation speed, and plunging force). This led to a dataset of almost 30 (joining time) × 60 (joining conditions) = 1800 records. This information was used to populate a database that was used to train, validate, and test the Artificial Neural Network model, as schematically depicted in Fig. 5.

3. Results

3.1. Effect of process parameters on frictional power

Fig. 6 depicts the influence of the tool rotation speed on the frictional power during the process. The trends indicate that the increase ω produces an increase in frictional power. However, for ω = 2000 RPM, the power showed a first initial steep increase, as long as the plunging force increased up to the prescribed load (500 N). Then, the power showed a knee and then a plateau [14]. On the other hand, for higher rotation speeds (ω = 4000 RPM, 6000 RPM, and 8000 RPM), the frictional power showed different trends. After the first peak, which increased with the rotation speed, the power tended to decrease during the dwell time. This was due to the metal and polymer softening that partially reduced the frictional heat (and power).

The influence of the mean plunging force and tool diameter on the frictional power variation during the process is reported in Fig. 7. These curves pertain to the same rotation speed (ω = 6000 RPM). These trends indicate the increase of the frictional power with the plunging force, regardless of the tool diameter. Higher plunging forces involved higher pressure, which in turn led to higher frictional power. Similarly, the increase in the tool diameter involved higher friction. Indeed, considering a sliding condition between the tool and the metal surface, the frictional heat Q produced by a flat tool with diameter D, a tool rotation ω, a coefficient of friction μ, and a pressure p is given by Eq. (2) [51,52]:

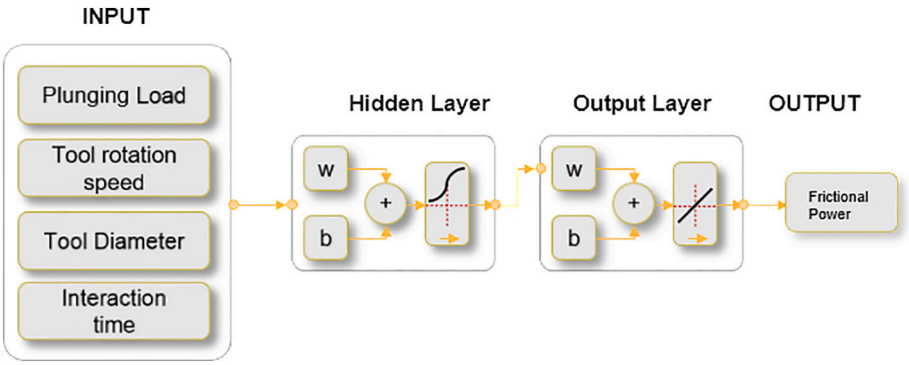

Fig. 4. Schematic of the Artificial Neural Network model structure.

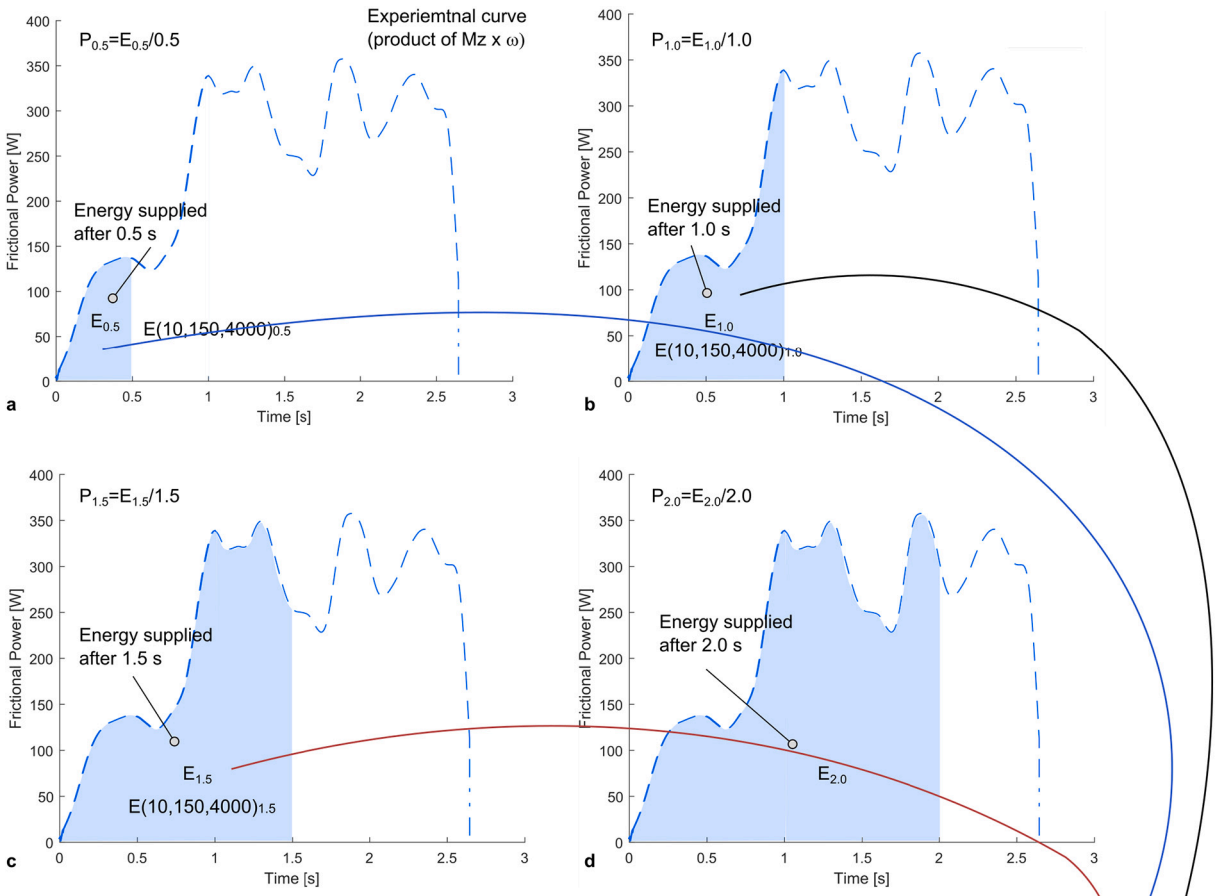

Database Structure

ID	Tool diameter, D [mm]	Plunging Force, F_{max} [N]	Rotation speed, ω [RPM]	Dwell time, D. [s]	Energy [J]
1	10	150	4000	0.5	$E(10,150,4000)_{0.5}$
2	10	150	4000	1	$E(10,150,4000)_{1.0}$
3	10	150	4000	1.5	$E(10,150,4000)_{1.5}$
	.	.	.		
	.	.	.		
30	10	150	4000	15	$E(10,150,4000)_{15}$
31	10	250	4000	0.5	$E(10,250,4000)_{0.5}$
	.	.	.	.	.
	.	.	.	.	.
	.	.	.	.	.
1800					$E(20,550,8000)_{15}$

Fig. 5. Typical power variation curve calculated through Eq. (1) using experimental measurements of the torque Mz, and data extraction. Mean power after (a) 0.5 s; (b) 1.0 s; (c) 1.5 s and (d) 2.0 s.

$$Q = \frac{2}{3}\cdot\pi\cdot\mu\cdot p\cdot\left(\frac{D}{2}\right)^3 \tag{2}$$

If F is the plunging force,

$$p = \frac{F}{\pi\cdot\left(\frac{D}{2}\right)^2} \tag{3}$$

Therefore, the frictional heat is

$$Q = \frac{2}{3}\cdot\pi\cdot\mu\cdot p\cdot\left(\frac{D}{2}\right)^3 = \frac{2}{3}\cdot\pi\cdot\mu\cdot\frac{F}{\pi\cdot\left(\frac{D}{2}\right)^2}\cdot\left(\frac{D}{2}\right)^3 = \frac{1}{3}\cdot\mu\cdot F\cdot D \tag{4}$$

Eq. (4) indicates that larger tools would involve higher frictional heat. Deep differences existed between the tests performed with different tools in terms of power variation during the joining time. The tests performed with tool diameters D = 10 mm and D = 15 mm were generally characterized by an almost constant frictional power. On the other hand, the tests performed using the larger tool (except those involving a plunging force of 150 N) showed a tendency of the frictional

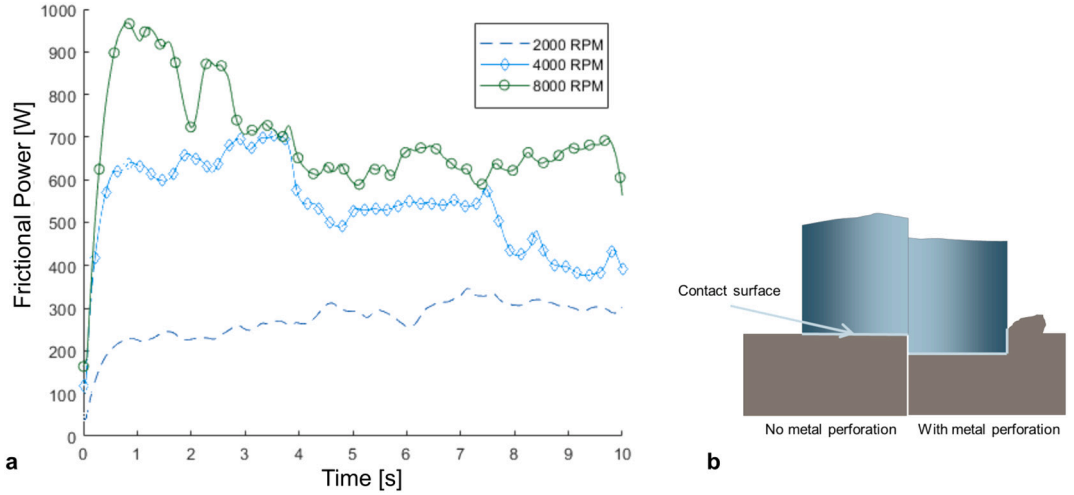

Fig. 6. (a) Influence of the rotation speed on the frictional power as measured experimentally (D = 15 mm, F_{max} = 500 N); (b) variation of the contact surface when the metal is plunged by the tool.

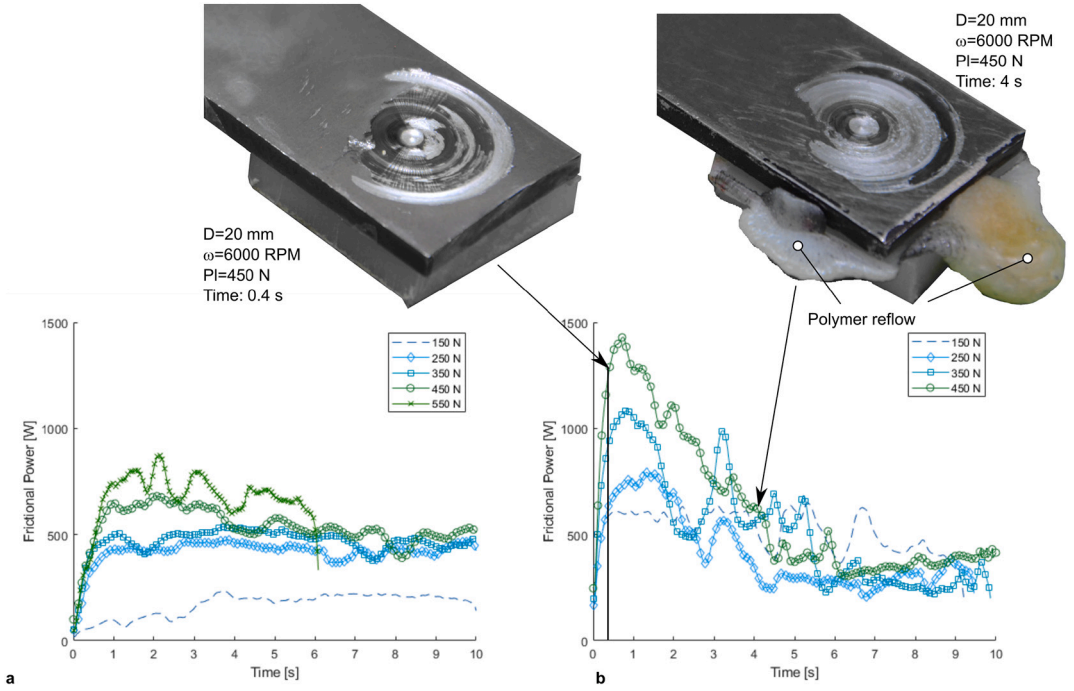

Fig. 7. Influence of Plunging force and tool diameter on the frictional power as measured experimentally. (a) D = 15 mm and (b) D = 20 mm. ω = 6000 PRM.

power to decrease after reaching a peak value. This difference was still due to the polymer softening that reduced the frictional power. Indeed, as a thick layer of polymer melted, this started to flow (leading to the polymer sheet thinning) causing a steep reduction of the frictional heat. This confirmed that the frictional power was highly influenced by the flow stress of the material involved.

Fig. 8 depicts the variation of the frictional power for different tool diameters and plunging forces. The above observations indicate that the processing conditions involving a mean frictional power lower than 600 N showed a more regular behavior (lower reduction of frictional power during the process). On the other hand, processing conditions leading to higher values of the frictional power involved a steeper reduction of the frictional power after reaching the peak value.

The trends of the plunging force confirm that after reaching the preset value, the plunging force held constant over time. On the contrary, the power can show great variations in time according to the process parameters adopted and severe variation of the material's flow stress.

The above results indicate that all the involved process parameters severely influenced the frictional power trends. Some of these factors showed a direct influence, e.g. the increase of the rotation speed involved a linear increase of the frictional power as long as both the metal and the polymer can bear the plunging force. On the other hand, other process parameters, e.g. the plunging force, the dwell time, and the tool diameter showed a more complex interwoven influence. This increases the difficulty to develop closed-form analytical or empirical models for power forecasting. This pushed to the development of the Artificial Neural Network relationship between the process parameters and the frictional power.

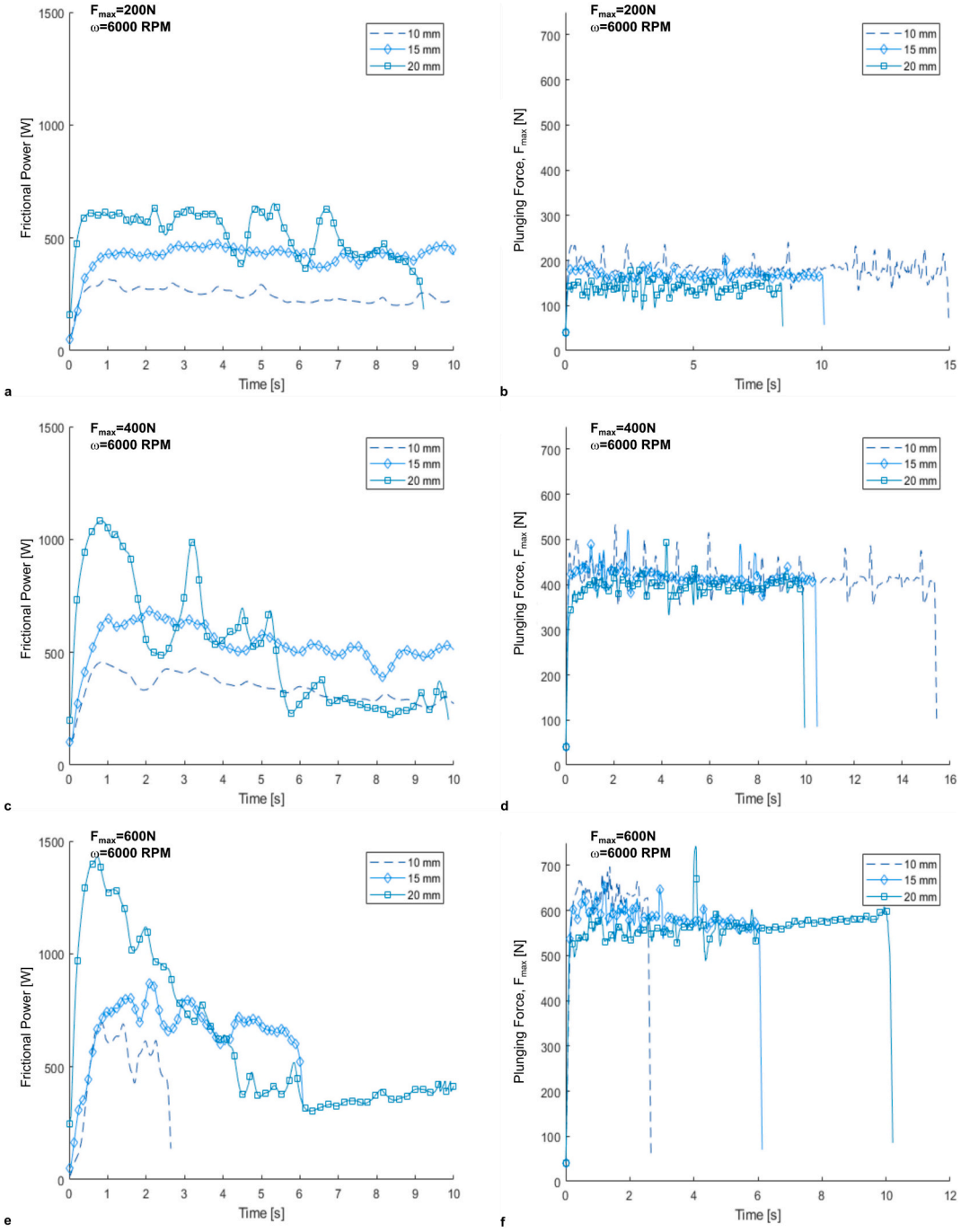

Fig. 8. Influence of tool diameter D and plunging force, F_{max} on frictional power, (a–b) 200 N, (c–d) 400 N, (e–f) 600 N.

Table 3
ANN models characteristics and evaluation of error estimators.

ID NET	Number of neurons 1st layer	Number of neurons 2nd layer	Mean [W]	STD. DEV. [W]	Coefficient of determination R^2
ANN1	5	5	41	61	0.899
ANN2	10	10	40	64	0.890
ANN3	20	20	37	70	0.905

3.2. Machine learning model predictions

Table 3 compares the mean and standard deviation values of the error of different Neural Networks which differ by the number of neurons within the hidden layers. These error estimators were calculated as the difference between the experimental measurement and the Artificial Neural Network prediction of the power over the entire dataset (almost 1800 samples). As expectable, increasing the number of neurons within the hidden layers increased the capability of the model to get closer to the experimental data (the mean error slightly reduced with an increase of the number of neurons, while the coefficient of determination R^2 slightly increases). However, this was done at the expense of model generalization, which is the capability to avoid overfitting.

A further comparison of the developed Artificial Neural Networks is depicted in Fig. 9. Here, the model error probability plot of the three network configurations is compared. Fig. 9 indicates a substantial equivalence among the network's accuracy. The statistical quality assessment predictors confirm such equivalence, thereby the simpler

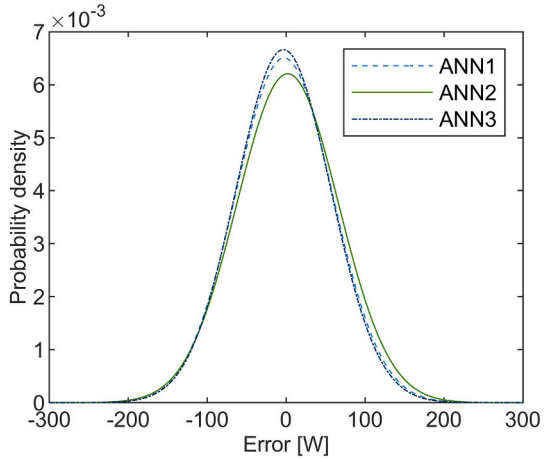

Fig. 9. Distribution of error affecting different Artificial Neural Networks configurations.

Artificial Neural Network (ANN1) was chosen as the higher generalization capability.

The above ANN1 was used to construct the response maps (reported in Fig. 10) that describe the relationship between the process parameters and the frictional power. Fig. 10a indicates the tendency of the frictional power to increase with the plunging force and the rotation speed. However, while the increase with the rotation speed is almost monotonic, the increase of the frictional power with the plunging force shows a plateau. For plunging forces higher than 400 N, the increase in the plunging force does not involve significant variation of the frictional power. This phenomenon was addressed to a severe aluminum reflow that was observed when the tool with smaller diameter D = 10 mm was used in conjunction with high plunging forces.

When the tools with larger diameters were used (D = 15 mm, and D = 20 mm), the frictional power still showed a tendency to increase with the plunging force and the rotation speed, as shown in Fig. 10b–c. However, the maps concerning D = 15 mm and D = 20 mm did not show the plateau. This was due to the lower pressure exerted by the tool on the underlying aluminum (as larger contact areas were involved). Thus, even under heavier conditions (higher plunging force and higher rotation speeds), the material reflow, which limits the plunging force, did not occur for diameters D = 15 mm and D = 20 mm.

The results also indicate that larger tools enabled to provide higher frictional power as higher torque was demanded, in agreement with Eq. (4).

In analogy to laser processes, the response surfaces of mean frictional specific power were calculated by dividing the power by the contact area (the surface area of the tool tip), as shown in Fig. 10d–f. It is worth noting that this is only a reference value as the frictional power is uneven under the tool-metal contact surface [16]. The temperature is highly dependent on the frictional specific power. The comparison between Fig. 10d–f shows that the increase in the diameter of the tool involved lower frictional specific power. For instance, the peak of frictional specific power reached with a diameter D = 10 mm was about 6.4 W mm^{-2}. This value drops to 3.7 W mm^{-2} (Fig. 10e) for a tool with diameter of D = 20 mm.

Fig. 11 analyses the interactions between the plunging force and the dwell time, as the rotation speed of the punch diameter changes. When using the tool with a diameter D = 10 mm, the increase in dwell time led to an increase in the average frictional power. This increase was attributed to the aluminum reflow that increased the contact area between the tool and the metal sheet.

The use of the tool with a diameter D = 20 mm involved different trends. For longer dwell time, the average power reduced as shown in Fig. 11g–i. This behavior was ascribed to the sharp variation of frictional Power shown in Fig. 7and Fig. 8e, especially when high plunging forces were adopted. The use of the tool with intermediate dimensions (D = 15 mm) shows an intermediate behavior between the tools with diameters D = 10 mm and D = 20 mm. In this case, the frictional power did not change with the dwell time.

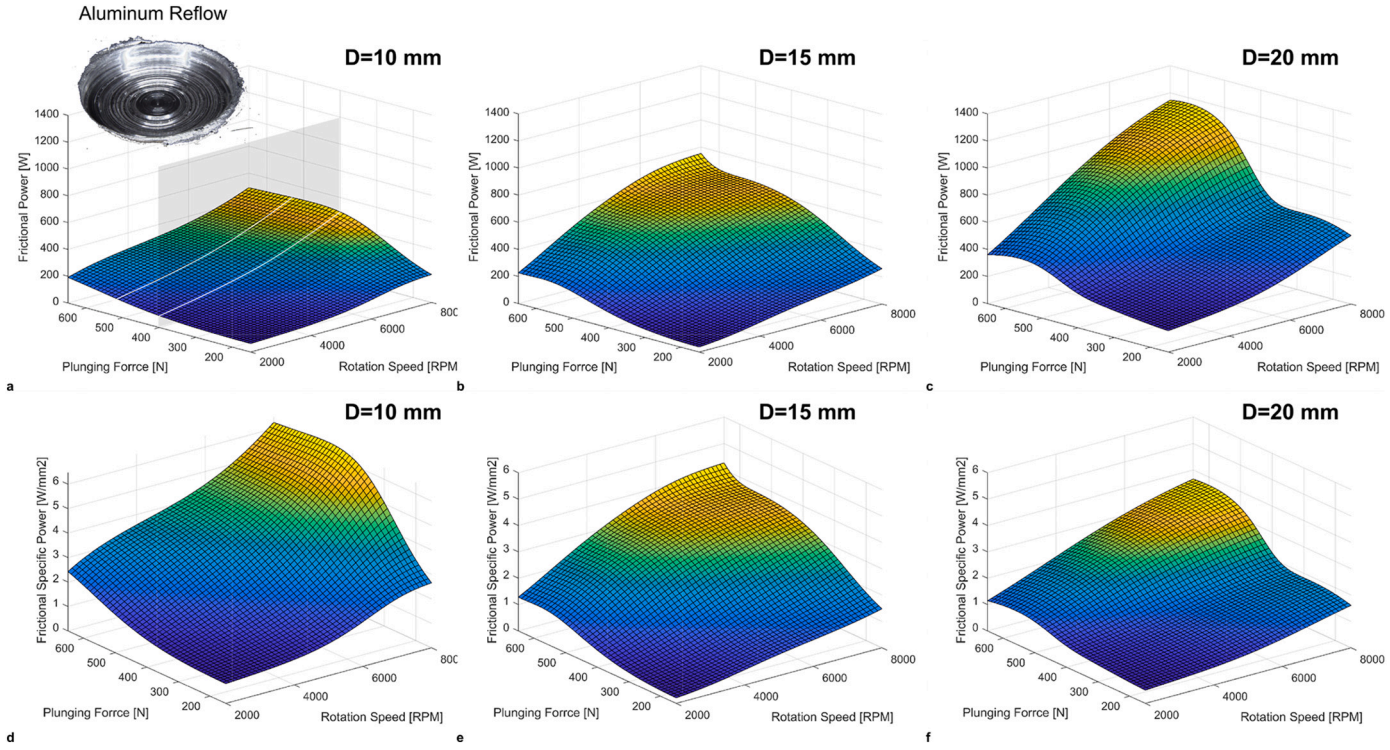

Fig. 10. Predicted response surface: influence of plunging force and rotation speed on frictional power (D_t = 1 s) using different tool diameters: (a)(d)D = 10; (b)(e) D = 15; and (c)(f) D = 20 mm.

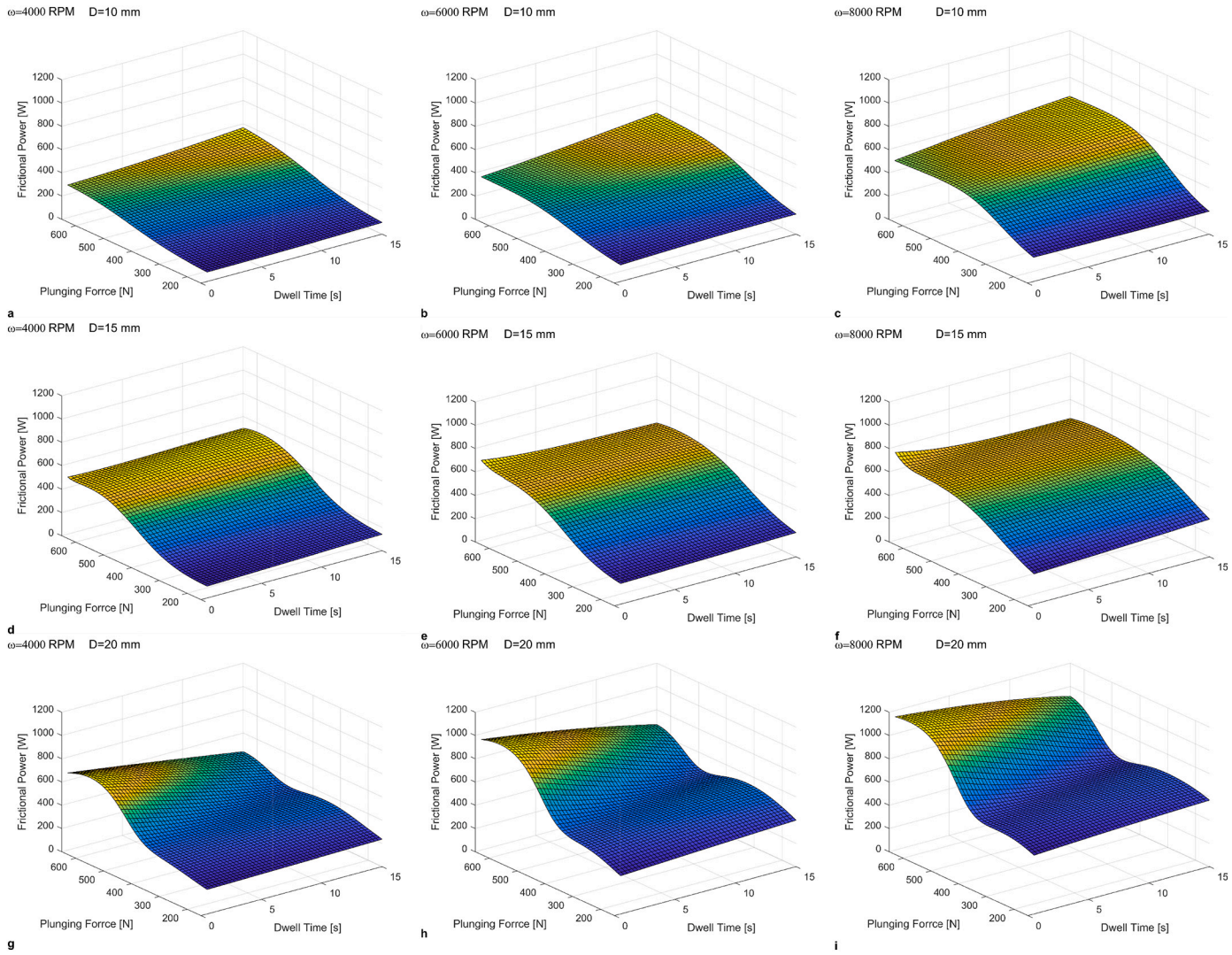

Fig. 11. Predicted response surface: influence of plunging force and dwell time on the frictional power using different tool diameters and rotation speeds.

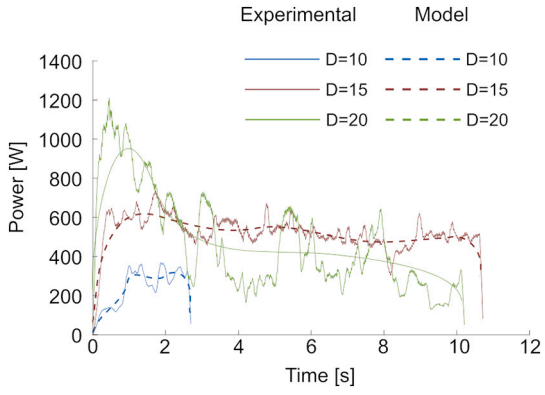

Fig. 12. Comparison of experimental and predicted power trends using different tool dimaters (ω = 4000 RPM, F_{max} = 600 N).

These trends are also depicted in Fig. 12, where the predicted values (Model) are compared to experimentally measured values (calculated as the torque by the rotation speed). It must be concerned that all the three curves were not used for training the ANN, but rather they were provided for validating the network. This comparison further indicates the good capability of the developed model to predict the power trends under different conditions.

4. Discussion

Friction-assisted joining enables the production of high-strength joints of dissimilar materials with simple equipment, in a short time, and reduced cost. When applied to join metals to thermoplastics or fiber-reinforced thermoplastics, the temperature at the metal-polymer interface triggers the successful joint formation [15]. Previous studies [16] demonstrated the close relationship between temperature and the frictional power involved in the process. However, unlike other joining processes such as direct laser joining, in frictional-based processes, the supplied power (frictional power) is not an input process parameter. Rather, it derives from the selection/combination of the process parameters such as plunging force, rotation speed, and tool diameter. Besides, the power can vary during the process since the severe change of the material behavior.

A machine learning approach was developed to predict frictional power based on the selection of the process parameters. To this end, a comprehensive campaign of experimental tests was conducted varying the main process parameters. The results indicated that there is a non-negligible interaction among the process parameters. This renders the prediction of the frictional power using analytical and traditional empirical models extremely complex. This is mainly due to the change of

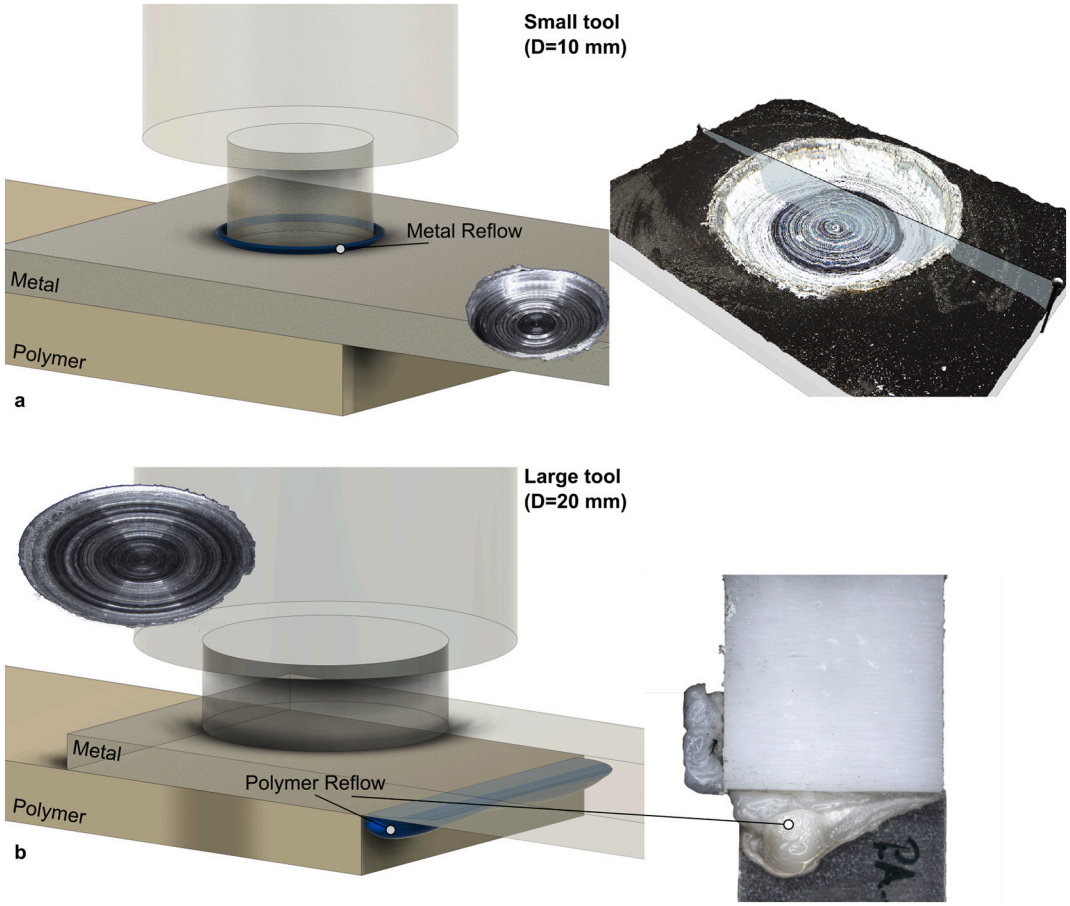

Fig. 13. Schematic of material reflow when (a) small and (b) large tools are adopted.

material behavior during the process. The model predictions were in good agreement with the experimental measurements. This was indicated by an average model error of almost 40 W and a coefficient of determination $R^2 \cong 0.90$. Also, great care was taken to model generalization, by avoiding overfitting.

In all the cases, the plunging force showed a lower influence on the frictional power than the tool rotation speed. This is particularly important in terms of process design and machine selection. Indeed, higher speeds would lead to a higher power and would be preferable to higher plunging forces. Besides, lower plunging forces would require lighter and more flexible equipment as lower forces are involved. Finally, lower plunging forces would involve shallower indentations left by the tool on the upper surface of the metal sheet, which leads to a better aesthetical appearance of the joints.

Although the influence of the plunging force on the frictional power was expectable, the adoption of larger tools represents the principal way that enables to increase the frictional power during the friction-assisted joining process. Besides, it would also increase the dimension of the joined area and consequently increase the load-bearing capability. When relatively small tools were adopted, high plunging forces and/or rotation speed should be avoided to prevent metal perforation. Consequently, the adoption of a larger tool enables to spread of the plunging force over a larger area reducing the contact stress at the tool-metal interface.

Fig. 13 further schematizes the influence of the tool diameter on the material flow. Small tools involve higher pressure that may lead to metal reflow and surface perforation. On the other hand, when larger tools are adopted, this issue is avoided as the larger contact area. Larger tools involved higher power supplied during the process. This led to higher heating of the polymer upper surface, which shortly approaches the melting/softening point. Consequently, the reduced polymer viscosity leads to the (unnecessary) ejection of a thin layer of material (polymer), as schematized in Fig. 13b.

5. Conclusions

The frictional power during the friction-assisted joining is not input data (such as laser direct joining) but rather it depends on the selection of the process parameters. The power also varies during the process owing to the variation of the metal flow stress and the contact tool-metal surface, metal reflow as well as polymer softening/melting. The developed machine learning model was capable to capture the influence of the process parameters (the tool diameter, the rotation speed, the plunging force, and dwell time) on the mean power supplied. The main achievements of the study are summarized as follows:

- The influence of the processing parameters on the mean frictional power was determined. The smaller tool involved lower power (650 W) but the highest power density (6.4 W mm^{-2}) while the larger tool involved almost double power (1150 W) and half power density (3.7 W mm^{-2}).
- The developed Machine Learning model was characterized by good reliability, as indicated by the key model indicators: $R^2 = 0.90$ and average temperature error of 40 W. The developed Machine Learning model was also capable to capture the steep variation of the frictional power with the interaction time. Also, great generalization capability was obtained as the predicted surface maps showed a regular behavior without falling in experimental data overfitting.
- the proposed signal breakdown approach was based on the time subdivision of the experimental measurements. This enabled to

development of a reliable Artificial Neural Network model with a limited number of testing conditions (60). Indeed, each power-time curve provided 30 experimental data leading to a sufficient number of records for training, validation, and testing the developed Artificial Neural Network.

Declaration of competing interest

The authors declare that they have no known competing financial interests or personal relationships that could have appeared to influence the work reported in this paper.

Acknowledgments

The authors would like to thank Mr. Giuseppe Organtini (DIIIE, University of L'Aquila) for his contribution during the setup and performance of the experimental tests.

References

[1] Amancio-Filho ST, Santos JF dos. Joining of polymers and polymer-metal hybrid structures: recent developments and trends. Polym Eng Sci 2009;49:1461–76.
[2] Lambiase F, Scipioni SI, Lee CJ, Ko DC, Liu F. A state-of-the-art review on advanced joining processes for metal-composite and metal-polymer hybrid structures. Materials 2021;14.
[3] Liu FC, Dong P, Lu W, Sun K. On formation of Al O C bonds at aluminum/polyamide joint interface. Appl Surf Sci 2019;466:202–9.
[4] Yusof F, Muhamad M, Moshwan R, Jamaludin M, Miyashita Y. Effect of surface states on joining mechanisms and mechanical properties of aluminum alloy (A5052) and polyethylene terephthalate (PET) by dissimilar friction spot welding. Metals 2016;6:101.
[5] Zhang Z, Shan J-G, Tan X-H, Zhang J. Effect of anodizing pretreatment on laser joining CFRP to aluminum alloy A6061. Int J Adhes Adhes 2016;70:142–51.
[6] Yusof F, Yukio M, Yoshiharu M, Shukor MH Abdul. Effect of anodizing on pulsed Nd:YAG laser joining of polyethylene terephthalate (PET) and aluminium alloy (A5052). Mater Des 2012;37:410–5.
[7] Aliasghari S, Ghorbani M, Skeldon P, Karami H, Movahedi M. Effect of plasma electrolytic oxidation on joining of AA 5052 aluminium alloy to polypropylene using friction stir spot welding. Surf Coat Technol 2017;313:274–81.
[8] Liu FC, Liao J, Gao Y, Nakata K. Effect of plasma electrolytic oxidation coating on joining metal to plastic. Sci Technol Weld Join 2015;20:291–6.
[9] Rodríguez-Vidal E, Sanz C, Soriano C, Leunda J, Verhaeghe G. Effect of metal micro-structuring on the mechanical behavior of polymer–metal laser T-joints. J Mater Process Technol 2016;229:668–77.
[10] Pardal G, Meco S, Dunn A, Williams S, Ganguly S, Hand DP, et al. Laser spot welding of laser textured steel to aluminium. J Mater Process Technol 2017;241:24–35.
[11] Wirth FX, Fuchs AN, Rinck P, Zaeh MF. Friction press joining of laser-texturized aluminum with fiber reinforced thermoplastics. Adv Mater Res 2014;966-967:536–45.
[12] Ye Y, Zou Q, Xiao Y, Jiao J, Du B, Liu Y, et al. Effect of interface pretreatment of Al alloy on bonding strength of the laser joined Al/CFRTP butt joint. Micromachines 2021;12:179.
[13] Schricker K, Samfaß L, Grätzel M, Ecke G, Bergmann JP. Bonding mechanisms in laser-assisted joining of metal-polymer composites. J Adv Joining Process 2020;1:100008.
[14] Lambiase F, Paoletti A. Mechanical behavior of AA5053/polyetheretherketone (PEEK) made by friction assisted joining. Compos Struct 2018;189:70–8.
[15] Lambiase F, Genna S, Kant R. Optimization of laser-assisted joining through an integrated experimental-simulation approach. Int J Adv Manuf Technol 2018;97:2655–66.
[16] Lambiase F, Di Ilio A, Paoletti A. Hybrid numerical modeling of friction assisted joining. J Manuf Process 2020;57:233–43.
[17] Lambiase F, Grossi V, Paoletti A. Defects formation during friction assisted joining of metals and semi crystalline polymers. J Manuf Process 2021;62:833–44.
[18] Ma N, Geng P, Ma Y, Shimakawa K, Choi J-W, Aoki Y, et al. Thermo-mechanical modeling and analysis of friction spot joining of Al alloy and carbon fiber-reinforced polymer. J Mater Res Technol 2021;12:1777–93.
[19] Lambiase F, Grossi V, Paoletti A. Machine learning applied for process design of hybrid metal-polymer joints. J Manuf Process 2020;58:92–100.
[20] Katayama S. Handbook of laser welding technologies. Woodhead Publishing; 2013.
[21] Franco G Di, Fratini L, Pasta A. Influence of the distance between rivets in self-piercing riveting bonded joints made of carbon fiber panels and AA2024 blanks. Mater Des 2012;35:342–9.
[22] Franco G, Fratini L, Pasta A, Ruisi AF. On the self-piercing riveting of aluminium blanks and carbon fibre composite panels. Int J Mater Form 2010;3:1035–8.
[23] Meschut G, Gude M, Augenthaler F, Geske V. Evaluation of damage to carbon-fibre composites induced by self-pierce riveting. Proc CIRP 2014;18:186–91.
[24] Mandel M, Krüger L. Electrochemical corrosion studies and pitting corrosion sensitivity of a self-pierce rivet joint of carbon fibre reinforced polymer (CFRP) – laminate and EN AW-6060-T6. Mater Werkst 2012;43:302–9.
[25] Lambiase F, Balle F, Blaga L-A, Liu F, Amancio-Filho ST. Friction-based processes for hybrid multi-material joining. Compos Struct 2021;266:113828.
[26] Yeh R-Y, Hsu R-Q. Development of ultrasonic direct joining of thermoplastic to laser structured metal. Int J Adhes Adhes 2016;65:28–32.
[27] Lionetto F, Balle F, Maffezzoli A. Hybrid ultrasonic spot welding of aluminum to carbon fiber reinforced epoxy composites. J Mater Process Technol 2017;247:289–95.
[28] Lionetto F, Mele C, Leo P, D'Ostuni S, Balle F, Maffezzoli A. Ultrasonic spot welding of carbon fiber reinforced epoxy composites to aluminum: mechanical and electrochemical characterization. Compos Part B Eng 2018;144:134–42.
[29] Krüger S, Wagner G, Eifler D. Ultrasonic welding of metal/composite joints. Adv Eng Mater 2004;6:157–9.
[30] Balle F, Eifler D. Statistical test planning for ultrasonic welding of dissimilar materials using the example of aluminum-carbon fiber reinforced polymers (CFRP) joints. Mater Werkst 2012;43:286–92.
[31] Wagner G, Balle F, Eifler D. Ultrasonic welding of aluminum alloys to fiber reinforced polymers. Adv Eng Mater 2013;15:792–803.
[32] Balle F, Huxhold S, Emrich S, Wagner G, Kopnarski M, Eifler D. Influence of heat treatments on the mechanical properties of ultrasonic welded AA 2024/CF-PA66-joints. Adv Eng Mater 2013;15:837–45.
[33] Magin J, Balle F. Solid state joining of aluminum, titanium and their hybrids by ultrasonic torsion welding. Mater Werkst 2014;45:1072–83.
[34] Staab F, Balle F. Ultrasonic torsion welding of ageing-resistant Al/CFRP joints: properties, microstructure and joint formation. Ultrasonics 2019;93:139–44.
[35] Junior WS, Handge UA, Santos JF dos, Abetz V, Amancio-Filho ST. Feasibility study of friction spot welding of dissimilar single-lap joint between poly(methyl methacrylate) and poly(methyl methacrylate)-SiO2 nanocomposite. Mater Des 2014;64:246–50.
[36] Goushegir SM, Santos JF dos, Amancio-Filho ST. Friction spot joining of aluminum AA2024/carbon-fiber reinforced poly(phenylene sulfide) composite single lap joints: microstructure and mechanical performance. Mater Des 2014;54:196–206.
[37] Esteves JV, Goushegir SM, Santos JF dos, Canto LB, Hage E, Amancio-Filho ST. Friction spot joining of aluminum AA6181-T4 and carbon fiber-reinforced poly (phenylene sulfide): effects of process parameters on the microstructure and mechanical strength. Mater Des 2015;66:437–45.
[38] Goushegir SM, Santos JF dos, Amancio-Filho ST. Influence of process parameters on mechanical performance and bonding area of AA2024/carbon-fiber-reinforced poly(phenylene sulfide) friction spot single lap joints. Mater Des 2015;83:431–42.
[39] Amancio-Filho ST, Bueno C, Santos JF dos, Huber N, Hage E. On the feasibility of friction spot joining in magnesium/fiber-reinforced polymer composite hybrid structures. Mater Sci Eng A 2011;528:3841–8.
[40] Yusof F, Miyashita Y, Seo N, Mutoh Y, Moshwan R. Utilising friction spot joining for dissimilar joint between aluminium alloy (A5052) and polyethylene terephthalate. Sci Technol Weld Join 2013;17:544–9.
[41] Huang Y, Meng X, Xie Y, Lv Z, Wan L, Cao J, et al. Friction spot welding of carbon fiber-reinforced polyetherimide laminate. Compos Struct 2018;189:627–34.
[42] Chen YJ, Yue TM, Guo ZN. Laser joining of metals to plastics with ultrasonic vibration. J Mater Process Technol 2017;249:441–51.
[43] Tamrin KF, Nukman Y, Zakariyah SS. Laser lap joining of dissimilar materials – a review of factors affecting joint strength. Mater Manuf Process 2013;28(8):857–71.
[44] Huang Y, Meng X, Xie Y, Li J, Si X, Fan Q. Improving mechanical properties of composite/metal friction stir lap welding joints via a taper-screwed pin with triple facets. J Mater Process Technol 2019;268:80–6.
[45] Huang Y, Meng X, Xie Y, Li J, Wan L. Joining of carbon fiber reinforced thermoplastic and metal via friction stir welding with co-controlling shape and performance. Compos A: Appl Sci Manuf 2018;112:328–36.
[46] Huang Y, Meng X, Wang Y, Xie Y, Zhou L. Joining of aluminum alloy and polymer via friction stir lap welding. J Mater Process Technol 2018;257:148–54.
[47] Blaga L, Bancilă R, Santos JF dos, Amancio-Filho ST. Friction riveting of glass–fibre-reinforced polyetherimide composite and titanium grade 2 hybrid joints. Mater Des 2013;50:825–9.
[48] Altmeyer J, dos Santos JF, Amancio-Filho ST. Effect of the friction riveting process parameters on the joint formation and performance of Ti alloy/short-fibre reinforced polyether ether ketone joints. Mater Des 2014;60:164–76.
[49] Meng X, Huang Y, Xie Y, Li J, Guan M, Wan L, et al. Friction self-riveting welding between polymer matrix composites and metals. Compos A: Appl Sci Manuf 2019;127:105624.
[50] Lambiase F, Paoletti A, Durante M. Mechanism of bonding of AA7075 aluminum alloy and CFRP during friction assisted joining. Compos Struct 2021;261:113593.
[51] Schmidt H, Hattel J, Wert J. An analytical model for the heat generation in friction stir welding. Model Simul Mater Sci Eng 2004;12:143–57.
[52] Essa ARS, Ahmed MMZ, Mohamed A-KYA, El-Nikhaily AE. An analytical model of heat generation for eccentric cylindrical pin in friction stir welding. J Mater Res Technol 2016;5:234–40.